Materials Today Bio 15 (2022) 100271

Contents lists available at ScienceDirect

Materials Today Bio

journal homepage: www.journals.elsevier.com/materials-today-bio

Biocompatible tellurium nanoneedles with long-term stable antibacterial activity for accelerated wound healing

Ling Huang [a,1], Meng Liu [d,1], Zhibin Feng [c], Xingyi Xu [a], Lingling Chen [c], Zhijun Ma [b,**], Lihua Li [a,*]

[a] The State Key Laboratory of Luminescent Materials and Devices, Guangdong Provincial Key Laboratory of Fiber Laser Materials and Applied Techniques, School of Materials Science and Technology, South China University of Technology, School of Physics, South China University of Technology, Guangzhou, Guangdong, 510640, China

[b] Zhejiang Lab, Research Center of Intelligent Sensing, China

[c] Guangdong Key Lab of Orthopedic Technology and Implant, General Hospital of Southern Theater Command of PLA, The First School of Clinical Medicine, Southern Medical University, Guangzhou, 510515, China

[d] Department of Orthodontics, Guanghua School of Stomatology, Hospital of Stomatology, Guangdong Provincial Key Laboratory of Stomatology, Sun Yat-sen University, Lingyuan West Road 56, Guangzhou, 510055, China

ARTICLE INFO

Keywords:
Tellurium nanoneedles
Antibacterial activity
Cytotoxicity
Wound healing

ABSTRACT

Tellurium (Te) nanomaterials (NMs) have emerged as a new antibacterial candidate to respond to the complex global health challenge of bacterial resistance. Herein, Te nanoneedles (NNs) that act both chemically and physically on bacteria are synthesized by a facile method using Na_2TeO_3, urea and glucose. It is found that the prepared Te NNs have a strong affinity to the cell membrane of bacteria and subsequently promote the generation of reactive oxygen species (ROS) in bacteria, resulting in an excellent antibacterial effect toward *Staphylococcus aureus* (Gram-positive) and *Escherichia coli* (Gram-negative). What's more, this needle-like morphology also can physically damage the bacterial cell membranes. The Te NNs per se are inert in mammalian cells to produce ROS at a proper concentration, indicating considerable biocompatibility of this material. As a proof-of-concept, the antibacterial Te NNs were used as an anti-inflammatory reagent for promoting bacteria-infected wound healing *in vivo*, during which Te NNs caused no evident side effects to major organs in mice. Additionally, the antibacterial activity is maintained in the presence of surface oxidation of Te NNs after long-term dispersion in phosphate buffered saline solution. The needle-like Te NMs with long-term antibacterial stability and good biocompatibility have great potential for the treatment of associated infectious diseases.

1. Introduction

Clinical operations such as prostheses replacement, dental operations, and open wounds have great risks in bacterial infections [1–5]. Although various antibiotics have been developed for solving these tough infections, the abuse of broad-spectrum antibiotics causes ever-increasing drug-resistance bacteria, which is currently one of the most daunting healthy crises for modern antibacterial medicine [6,7].

The merits of large surface-to-volume ratio, special morphology, low toxicity and facile surface functionalization ability confer nanomaterials (NMs) as rising stars for biomedical application, especially in the antibacterial field [8]. Various inorganic nanomaterials, such as Ag-based nanoparticles (NPs), Cu-based NPs, TiO_2 NMs, ZnO NMs and black/red phosphorus have been developed for anti-pathogenic microorganisms [9–17]. Those NPs could produce abundant reactive oxygen species (ROS) for bacterial killing by themselves or under external stimuli (laser, magnetic, light). Although the ROS make a great contribution to sterilization, it also poses a great threat to cells and tissues and will induce inflammatory responses during the therapeutic process [18,19]. To promote wound healing and kill bacteria at the same time, 2D materials such as black/red phosphorus nanosheets [15,17], $Ti_3C_2T_x$ MXene [20], graphitic carbon nitride-based materials [21–23] and metal-organic framework-based materials [24] have been developed recently. However, the synthesis of these nanomaterials is generally complicated, with

* Corresponding author.
** Corresponding author.
E-mail addresses: zhijma@zhejianglab.com (Z. Ma), li-hua.li@polyu.edu.hk (L. Li).
[1] These authors contributed equally.

https://doi.org/10.1016/j.mtbio.2022.100271
Received 17 January 2022; Received in revised form 13 April 2022; Accepted 25 April 2022
Available online 29 April 2022

low synthesis efficiency and high cost. Moreover, the need of external stimuli also limits the convenience of the application.

Elementary substance Te as a p-type semiconductor with band-gap energy of 0.35 eV, whose toxicity is much lower than other Te compounds, is recently recognized as a competitive candidate that can be used as antibacterial agents [25–27]. However, there has been no consensus on the antibacterial mechanism of the Te NPs. And notably, the tricky biofilms formed by bacteria, which support a more comfortable environment for bacterial attachment and growth and then become a "protective umbrella" for bacteria, are a core reason for repeated infection [28,29]. The biofilm destruction ability of Te NMs has rarely been explored. In addition, the variation in the antibacterial properties of Te NPs with the oxidation is well worthy of exploration since the Te NPs are easily oxidized in air as well as in solution [30,31].

In this work, we develop a facile one-step approach for the efficient synthesis of Te nanoneedles (NNs). It is found that the Te NNs can efficiently attach to the surface of *S. aureus* and *E. coli* to directly promote the generation of ROS in bacteria without external excitation required, which causes the irreversible destruction of membrane structure and deoxyribose nucleic acid (DNA), leading to the death of the bacterial cells. Moreover, the Te NPs are provided with needle-like structure that can puncture bacterial membranes and then cause physical damage. The prepared Te NNs exhibit retained chemical and physical damage to bacteria during long-term exposure of 25 days. Noteworthy, the Te NNs themselves are inert to produce ROS and will not stimulate mammalian cells to generate ROS at proper doses, resulting in excellent biocompatibility. Interestingly, Te NNs or surface oxidized Te NNs (Te–SO NNs) exhibit similar antibacterial activity against *Staphylococcus aureus* (*S. aureus*) and *Escherichia coli* (*E. coli*). We further explore the antibacterial ability and wound healing efficiency of Te NNs *in vivo*, the results show that they can effectively eliminate bacteria and significantly accelerate healing of *S. aureus*-infected and *S. aureus* & *E. coli* co-infected wounds. Therefore, these biocompatible Te NNs could work as a promising candidate to kill bacteria for the treatment of associated infectious diseases.

2. Experiments

2.1. Preparation and characterization of Te NNs and Te–SO NNs

The Te NNs were synthesized via a facile one-step method by reacting Na_2TeO_3, urea and glucose (analytical grade, Aladdin, Shanghai, China) at a ratio of 1:10:10 for 1 h at 80 °C [32–36]. Briefly, Na_2TeO_3 (10 mM, 50 mL) was dissolved in deionized water and stirred in a magnetic mixer at 80 °C, set as A solution. The mixture of urea and glucose (100 mM, 50 mL) was dissolved in deionized water, set as B solution. Then, B was added to A solution, after stirring for 15 min, NaOH (2 M, Aladdin, Shanghai, China) was subsequently added dropwise to adjust the pH value ~9. The mixed solution reacted under vigorous magnetic stirring at 80 °C for 1 h. After that, the container was cooled to room temperature naturally. The Te NNs synthesized above were washed several times with deionized water and ethanol. Finally, the products were dried in vacuum at 60 °C for characterization. Furthermore, the Te NNs were dispersed in the phosphate buffered solution (PBS, Sigma-Aldrich) for 14 days to form Te–SO NNs, and the products were also dried in vacuum at 60 °C for characterization.

The prepared Te and Te–SO NNs were characterized using a series of methods including HRTEM, XRD, Raman and XPS, etc. The NNs suspension was placed on a carbon-coated copper grid and observed using HRTEM (JEOL 2100, Japan). The X-ray diffraction (XRD) patterns of Te and Te–SO NNs were acquired using a Multi-position automatic sampling X-ray diffractometer (X'pert Powder, PANalytical) in the 2-theta range of 5°–90° under 40 kV and 30 mA, with $\lambda = 1.5406$ Å radiation. Raman spectra of Te and Te–SO NNs were recorded on a confocal Raman microscope (HJY LabRAM Aramis, France) with a 532 nm laser source at an output power of ~5 mW for excitation. The X-ray photoelectron spectra (XPS) of Te and Te–SO NNs were taken on a ThermoFisher ESCALAB Xi^+ with an incident monochromated X-ray beam from the Al target.

2.2. Cell culture and cytotoxicity in vitro

Murine fibroblast cells (L929) were selected to evaluate the cytotoxicity of the Te and Te–SO NNs by 3-(4,5-dimethylthiazol-2-yl)-2,5-diphenyltetrazolium bromide (MTT) assay. L929 cells (100 μL) were seeded into a respective 96-well plate at a density of 1×10^5 cells·cm^{-2} and cultured with Dulbecco's modification of Eagle's medium (DMEM, Gibco, USA) containing 10% fetal bovine serum (FBS, Sigma) and 1% penicillin-streptomycin (P/S). After the Te NNs were suspended in the PBS, gradient concentrations of 200, 100, 50, 25, 12.5, 6.25 and 0 μg mL^{-1} were added to the plates and co-cultured at 37 °C for 24 h. Then, cell proliferation was assessed by the MTT assay at 37 °C for 4 h. The formazan was then dissolved using dimethyl sulfoxide (DMSO, sigma, USA), and the optical density (OD) was measured at 490 nm using a microplate reader (Infinite 200 Pro). A certain concentration of Te NNs was dispersed in PBS for 14 d and then repeat the operation above to evaluate the cytotoxicity of the Te–SO NNs.

In addition, the visualized viability of the L929 cells was determined with a live/dead staining under the fluorescence microscope. The cells were cultured with the NNs (100 μg mL^{-1}) in 24-well plate for 24 h. At the end of the incubation period, the medium was removed and 250 μL Calcein-AM/PI staining solution (2 μM Calcein-AM and 4.5 μM PI in DMEM) was added into 24-well plate, then cultured for 20 min at 37 °C in darkness. Finally, the cells were washed gently with PBS at least three times and placed under a fluorescence microscope to record the cell growth on the Te NNs and Te–SO NNs.

2.3. In vitro antibacterial activity

The *S. aureus* and MRSA were grown in sterilized Nutrient-Broth (NB) medium (0.3% w/v beef extract, 0.5% w/v NaCl, 1% w/v tryptone). And the *E. coli* were grown in sterilized Luria-Bertani (LB) medium (0.5% w/v yeast extract, 0.5% w/v NaCl, 1% w/v tryptone) by using a shaking incubator at 150 rpm at 37 °C overnight. The bacterial concentration was defined by measuring the OD value at 600 nm, and $OD_{600} = 1$ was considered 5×10^8 CFU mL^{-1}. In the control group, the bacteria *S. aureus* (or MRSA) were adjusted to a concentration of 2×10^6 CFU mL^{-1} in PBS containing 3% NB and *E. coli* were diluted to the same concentration in PBS containing 1% LB. The concentrations of Te and Te–SO NNs (as well as Te NNs dispersed in PBS for 6 months) were varied from 0 to 100 μg mL^{-1} and then introduced to bacterial suspension. The resultant suspension was incubated in a biochemical incubator at 37 °C for 24 h. The bacteria culture suspension was diluted 1000 times in PBS and a suspension of 100 μL from each tube was uniformly spread on the NB agar plates and the number of viable bacterial colonies was counted after incubation at 37 °C for 24 h. To quantify the antibacterial ability, the bactericidal rate was calculated based on the following equation:

$$\text{Antibacterial rate}(\%) = (N_{control} - N_{NNs}) / N_{control} \times 100$$

Where $N_{control}$ is the average number of bacteria in the control sample (CFU/sample), and N_{NNs} is the average number of bacteria in the testing samples (CFU/sample). The minimum inhibitory concentration (MIC) is set as the lowest drug concentration that can inhibit the growth of 80% of pathogenic bacteria after 24 h of *in vitro* culture. Furthermore, the visualized viability of the bacteria treated with 100 μg mL^{-1} Te and Te–SO NNs was determined with SYTO 9/PI staining (SYTO 9 and PI, Thermo Fisher Scientific Co, Ltd, USA) at 37 °C for 30 min and then observed under confocal laser scanning microscope (CLSM).

To directly observe the morphology changes of bacteria after treated with Te and Te–SO NNs, scanning electron microscopy (SEM, ZEISS, Germany) was employed. After different treatments (as described above) and co-cultured for 24 h, the samples were gently rinsed with PBS and

fixed with 3% glutaraldehyde overnight. Then, the samples were subsequently dehydrated with 20, 40, 60, 80, 90, 95and 100% ethanol. The samples were dried naturally and coated with gold for SEM observation.

2.4. In vitro biofilm formation and antibiofilm ability to E. coli

For the formation of the biofilm, 1 mL of *E. coli* suspensions with $OD_{600} = 1$ were seeded on the surface of the sterilized Si plates and incubated in a 24-well plate at 37 °C. To further observe the antibiofilm ability of Te and Te–SO NNs, 100 μg mL^{-1} Te and Te–SO NNs were added to the bacterial suspension above. After 24 h of incubation, the Si plates were gently washed three times with PBS to remove the suspended bacteria and fixed with 3% glutaraldehyde overnight. Then, the samples were subsequently dehydrated with 20, 40, 60, 80, 90, 95 and 100% ethanol. Finally, the samples were dried naturally and coated with gold for SEM observation. In addition, the *E. coli* were seeded on the surface of the sterilized glass slides to form the biofilm as above. After *E. coli* biofilm co-cultured with Te and Te–SO NNs (100 μg mL^{-1}) for 2 h and 12 h, samples were gently rinsed twice with 1 mL of PBS to remove non-adherent planktonic bacteria. Samples were then incubated in 500 μL of 0.4% MTT solution at 37 °C for 3 h followed by dissolution of the purple formazan crystals in 500 μL of DMSO. Absorbance of the purple colored solution was measured at 490 nm using a microplate reader (Infinite 200 Pro).

2.5. Assessments of AMR evolution in bacteria

On the basis of the operation and results about *in vitro* antibacterial activity, 2×10^6 CFU mL^{-1} bacteria (*S.aureus* and *E. coli*) were inoculated into PBS containing 3% NB with dosages of 0.25 × MIC, 0.5 × MIC, 1 × MIC, 2 × MIC, 4 × MIC, 8 × MIC Te NNs. Next, after incubated for 24 h at 37 °C, it was spread on a nutrient plate to evaluate the sterilization effect. Then, the colonies of *S. aureus* and *E. coli* with a certain inhibitory effect on the growth but could ensure the basic growth of the bacteria were collected in culture and shaken for 4 h at 37 °C, and subsequently, repeat the above-mentioned cultivation operation. This continuous passage was repeated every day for 25 days.

2.6. Binding ability

Isothermal titration calorimetry (ITC) experiments were conducted with a MicroCal VP-ITC instrument at 25 °C. Lipopolysaccharide (LPS) solution, Peptidoglycan (PG) solution and the Te NNs solution were prepared in PBS. For a typical titration, 10 μL LPS or PG solution was injected into the Te NNs solution within a duration of 20 s. The spacing time between two continuous injections was 2 min. The heat for each injection was determined by the integration of the peak area in the thermogram corresponding with the reaction time.

2.7. Intracellular ROS generation

The *S. aureus* and *E. coli* suspension (2×10^6 CFU mL^{-1}) were given different treatments as described above. The 2,7-Dichlorodi-hydrofluorescein diacetate (DCFH-DA) stock solution (10 mM) was diluted with PBS to obtain the working solution (20 μM). The bacterial culture along with NNs suspension (100 μg mL^{-1} in PBS) were incubated with the DCFH-DA working solution at 37 °C for an additional 1 h, and the fluorescence intensity of samples was observed by fluorescence microscopy and detected by a microplate reader (Infinite 200 Pro) at 525 nm under the excitation of 488 nm.

The intracellular ROS production of L929 cells was also detected by DCFH-DA. In brief, L929 cells were seeded in culture dishes (1×10^5 cells·mL^{-1}) and cultured for 12 h. After washing with PBS three times, the cells along with DCFH-DA probe were incubated for 2 h with/without NNs (100 μg mL^{-1}). Finally, the cells were washed with PBS and observed under CLSM.

2.8. Bacterial genomic DNA integrity

After the bacteria with/without the treatment of NNs (100 μg mL^{-1}) were cultured for 24 h, genomic DNA was extracted using Bacteria DNA Kit (Solarbio, Beijing, China). The concentration and purity of the bacterial DNA were detected by Nano-Drop 2000 (Thermo Fisher Scientific, USA). Agarose gel was prepared with 1 × TAE buffer, and ethidium bromide (5 μL per 100 mL of the gel) was used to monitor the size of the analyzed fragment. Electrophoresis (Bio-Rad, Hercules, CA, USA) was run at 110 V for 30 min. The bands were visualized by a UV trans-illuminator (Bio-Rad, GDS-7500, USA).

2.9. In vivo anti-infection and wound healing

The permission for the animal experiments was obtained from the Institutional Animal Care and Use Committee (IACUC) of General Hospital of Southern Theater Command of PLA. Male Sprague-Dawley (SD) rats (~250–300 g) were purchased from Medical Experimental Animal Center of Guangdong Province. After being anesthetized with 3% pentobarbital at a dose of 45 mg kg^{-1} of body weight, the fur on the dorsum skin of the rat was shaved off, and the skin was sterilized using 0.5% iodophor for aseptic surgery. To establish the rat model of infectious wound, two full-thickness skin wounds (diameter≈15 mm) were excised using a sterile round cutaneous punch on the dorsal side skin. 10% (wt/v) polyvinyl alcohol (PVA) was dissolved in PBS and stirred in a magnetic mixer at 90 °C for 4 h to prepare PVA hydrogels. And the Te NNs suspension was mixed in PVA hydrogels to further form the Te NNs/PVA hydrogels (the concentration of Te NNs is 100 μg mL^{-1}). The rat model of infectious wound was divided into two series including *S. aureus* infected model and *S. aureus* & *E. coli* co-infected model. For *S. aureus* infected series, an *S. aureus* suspension (100 μL, 5×10^8 CFU mL^{-1}) was directly dropped on the wound and the wounds were covered with sterile gauze for 24 h. A total of 15 rats were randomly divided into three groups (5 rats per group): control group (treated with 100 μL PBS), PVA group (treated with 100 μL PVA hydrogel), and Te NNs/PVA group (treated with 100 μL Te NNs/PVA hydrogel). As to *S. aureus* and *E. coli* co-infected series, the procedure is the same as that of the *S. aureus* series apart from different bacterial suspension addition, in which an *S. aureus* and *E. coli* mixture (100 μL, 5×10^8 CFU mL^{-1}) was dropped on the wound instead of *S. aureus* suspension. Photographs of the wound on the mice during the wound healing process (day 0, 4, 7, 10, and 14) were recorded using a digital camera. And the wound area was quantified using image analysis software (Image J). The wound healing rate was calculated using the following equation:

$$\text{Wound healing rate}(\%) = (A_{initial} - A_{time}) / A_{initial} \times 100$$

Where $A_{initial}$ is the initial wound area (day 0), and A_{time} is the wound area at different time points.

In addition, bacteria were collected from the wounds and suspended in 1 mL PBS at days 4, 7, 10, and 14. The samples were diluted 10 times and 100 μL of the diluted solutions were spread on NB agar plates and incubated for 24 h at 37 °C. Then the number of bacterial colonies on agar plates was calculated using Image J software.

2.10. Histological analysis

Hematoxylin & eosin (H&E) staining and Masson's trichrome staining of the wound tissue after 7 and 14 days of treatment were performed to assess the wound recovery. The rats were sacrificed with an overdose of pentobarbital, after that the wound tissues with adjacent normal skin were harvested and fixed in the 4% paraformaldehyde solution for 24 h at 4 °C. After 14 days of different treatments, the major organs (heart, liver, spleen, lung, and kidney) were also collected and fixed for H&E staining.

2.11. Statistical evaluation

All quantitative tests were carried out at least in triplicate, and the data were expressed as mean ± standard deviation (SD). The statistical comparison was tested by Tukey's multiple comparisons test using SPSS (version 10; SPSS Inc, Chicago, IL). The value with $*p < 0.05$ were considered statistically significant, and $**p < 0.01$ were set as highly statically significant.

3. Results and discussion

3.1. Characterization

The TEM image in Fig. 1a shows the needle stick-like Te NNs with a diameter of ~40 nm, and lengths range from ~500 nm to even 1 μm. The electron diffraction pattern (inset of Fig. 1a) and HRTEM image (Fig. 1b) present the crystalline structure of the Te NNs with interplanar spacing d = 0.3218 nm, which is consistent with (101) plane of hexagonal tellurium crystal. Interestingly, the surface of Te NNs was oxidized after preserved in the PBS for 14 d, namely Te–SO with increased diameter to 100 nm (Fig. 1c). Fig. 1d illustrates the X-ray diffraction (XRD) patterns of the Te and Te–SO NNs, all peaks in the pattern of Te samples are in good agreement with the standard literature data (JCPDS: 36–1452). Notably, some peaks in Te–SO NN samples are attributed to orthorhombic TeO_2 (JCPDS: 74–1131) have appeared (star mark), which indicates that part of Te NNs are oxidized and therefore Te–SO NNs are formed. The Raman scattering spectra taken for the Te NNs and Te–SO NNs are depicted in Fig. 1e. The characteristic vibration peaks at 121.7 cm^{-1}, 141.1 cm^{-1} are observed in both Te and Te–SO samples, which are close to those reported Te NPs previously [37–39]. Moreover, the peaks at 180 cm^{-1}, 226 cm^{-1}, 444 cm^{-1}, 583 cm^{-1}, 650 cm^{-1} and 665 cm^{-1} which are attributed to β-TeO_2 [40] emerge in the Te–SO samples (star mark) due to surface oxidation, which is consistent with the XRD results above. Additionally, the characteristic XPS spectra (Te $3d_{5/2}$ and Te $3d_{3/2}$ peaks) further support the formation of Te and Te–SO NNs. In these XPS region spectra (Fig. 1f), the Te $3d_{5/2}$ and Te $3d_{3/2}$ peaks at 573.4 eV and 583.7 eV associated with Te (0) appear in the Te samples [38,41]. While the appearance of additional Te $3d_{5/2}$ and Te $3d_{3/2}$ peaks at 576.4 eV and 586.6 eV which arise from Te (IV) is observed in the Te–SO samples [42–44].

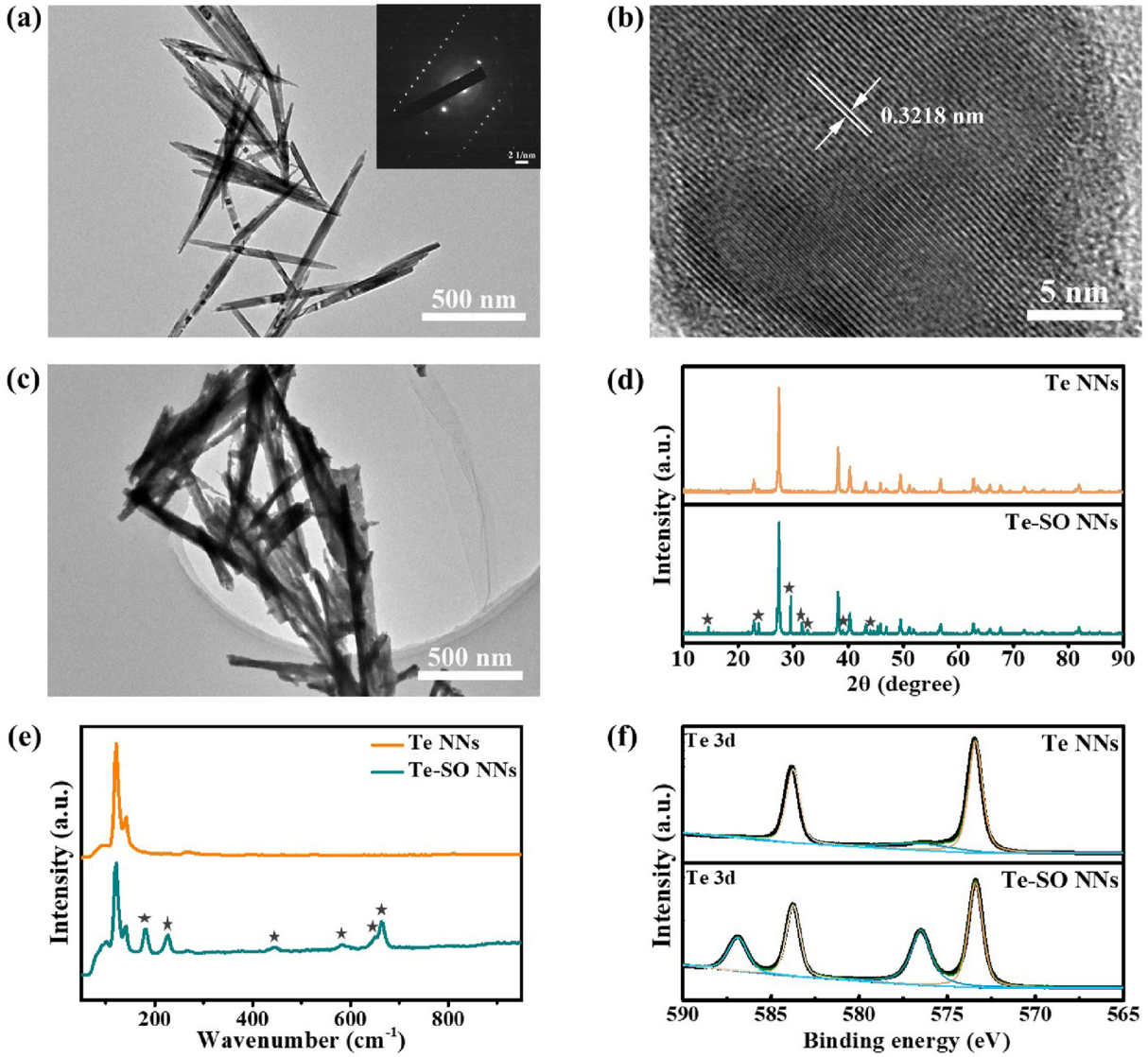

Fig. 1. Characterization of the Te and Te–SO NNs. (a) TEM image of the Te NNs; inset: Selected area electron diffraction (SAED) images. (b) HRTEM image of the Te NNs; the lattice spacing corresponds to (101) in XRD. (c) TEM image of the Te–SO NNs. (d) XRD pattern of the Te and Te–SO NNs. (e) The Raman spectra and (f) XPS spectra of the Te and Te–SO NNs.

3.2. In vitro cytotoxicity assessment

Cytotoxicity is the biggest concern in biomedical applications of biomaterials [45]. A proper dose of Te NNs can kill bacteria but not do harm to mammalian cells selected here. As shown in Fig. 2a, the cell viability is slightly lower than 80% when the concentration of Te or Te–SO NNs is up to 200 μg·mL^{-1}. When their concentrations are lower than 100 μg mL^{-1}, both Te NNs and Te–SO NNs have a negligible effect on the L929 cells. Subsequently, the L929 cells were stained with calcein-AM and propidium iodide (PI) to identify live and dead cells, respectively. The full-screen green fluorescence in the control group as well as NNs groups indicates the excellent biocompatibility of Te and Te–SO NNs (100 μg mL^{-1}). Furthermore, The ROS production in L929 cells is monitored using a green probe, DCFH-DA. As shown in Fig. 2c, L929 cells internalizing Te or Te–SO NNs exhibit negligible fluorescence along with the control group, illustrating the inert character of NNs, which further confirms their biocompatibility.

3.3. Antibacterial activity to S. aureus

We further explored the antibacterial ability of Te NNs and Te–SO NNs toward gram-positive bacteria (*S. aureus*). As shown in Fig. 3, Te NNs can kill all *S. aureus* at the concentration of 100 μg mL^{-1} and Te–SO NNs also exhibit excellent antibacterial properties toward *S. aureus* at the same concentration with an antibacterial rate of 98.2% (Fig. 3a and b). Nevertheless, when their concentration falls to 50 μg mL^{-1}, dozens of colonies can be observed on Te NNs as well as Te–SO NNs group (Fig. 3a), which indicates that the antibacterial ability is concentration-dependent. When the concentration further decrease to 25 μg mL^{-1}, Te NNs exhibit poor bactericidal effect. What's more, the antibacterial activity attenuates when oxidation occurs on the surface of Te NNs, which decreases from 87.6 to 78.2% at the concentration of 50 μg mL^{-1}. We set the lowest drug concentration that can inhibit the growth of 80% of pathogenic bacteria after 24 h of *in vitro* culture as the minimum inhibitory concentration (MIC). Therefore, the MIC of Te and Te–SO NNs to *S. aureus* are listed as 50 and 75 μg mL^{-1}, respectively. After a longer dispersion of 6 months, partially oxidized Te NNs also show bactericidal activity to *S. aureus* with the antibacterial rate of 100% at the concentration of 100 μg mL^{-1}, and MIC is listed at 12.5 μg mL^{-1} (Figure S1). Furthermore, as the treatment of multidrug-resistant bacteria is still an intractable health challenge, the antibacterial ability of Te and Te–SO NNs to one of the most serious superbugs—methicillinresistant *Staphylococcus aureus* (MRSA) is

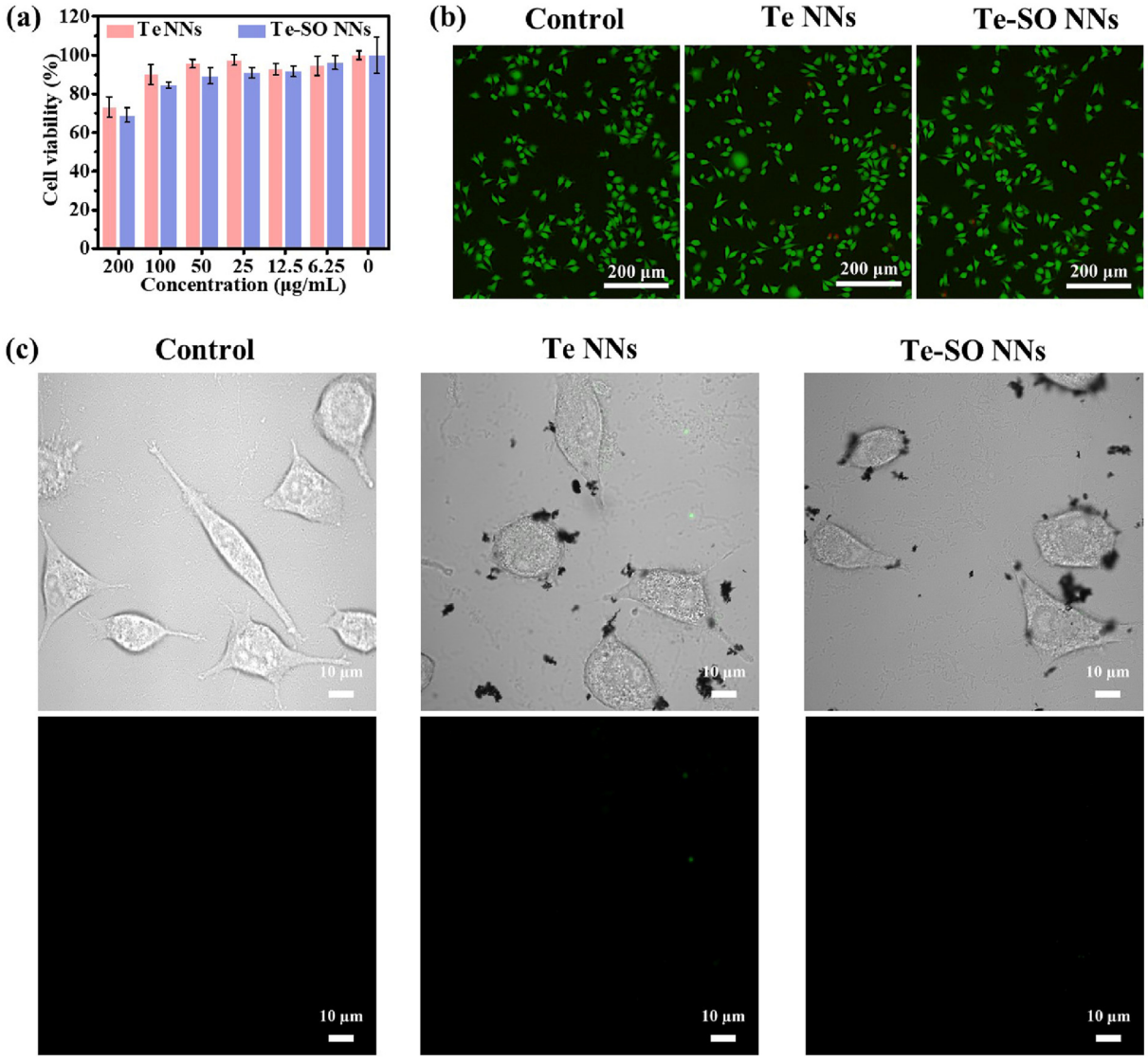

Fig. 2. Cytotoxicity of the Te and Te–SO NNs. (a) Cytotoxicity of L929 co-cultured with different concentrations of Te and Te–SO NNs; (b) Fluorescence images of the L929 cells after Live/Dead staining in the different groups; (c) Bright-field images and DCFH-DA fluorescence images of L929 cells with several treatments for detection of ROS level.

observed in Figure S2. Unfortunately, both Te and Te–SO NNs perform inferiorly in MRSA elimination even at the concentration of 100 μg mL^{-1}, with the antibacterial rate of only respective 72.27% and 66.91% (Figure S2a,b).

Considering the immediate and long-term antibacterial efficiency together, we choose 100 μg mL^{-1} Te NNs for further experiments and the effects of Te–SO NNs at the same concentration are simultaneously investigated. The *S. aureus* killing effect of NNs is further observed using bacterial SYTO 9/PI staining. SYTO 9 is a membrane-permeable dye that can enter all bacterial cells [28,29], whereas PI is excluded from cells

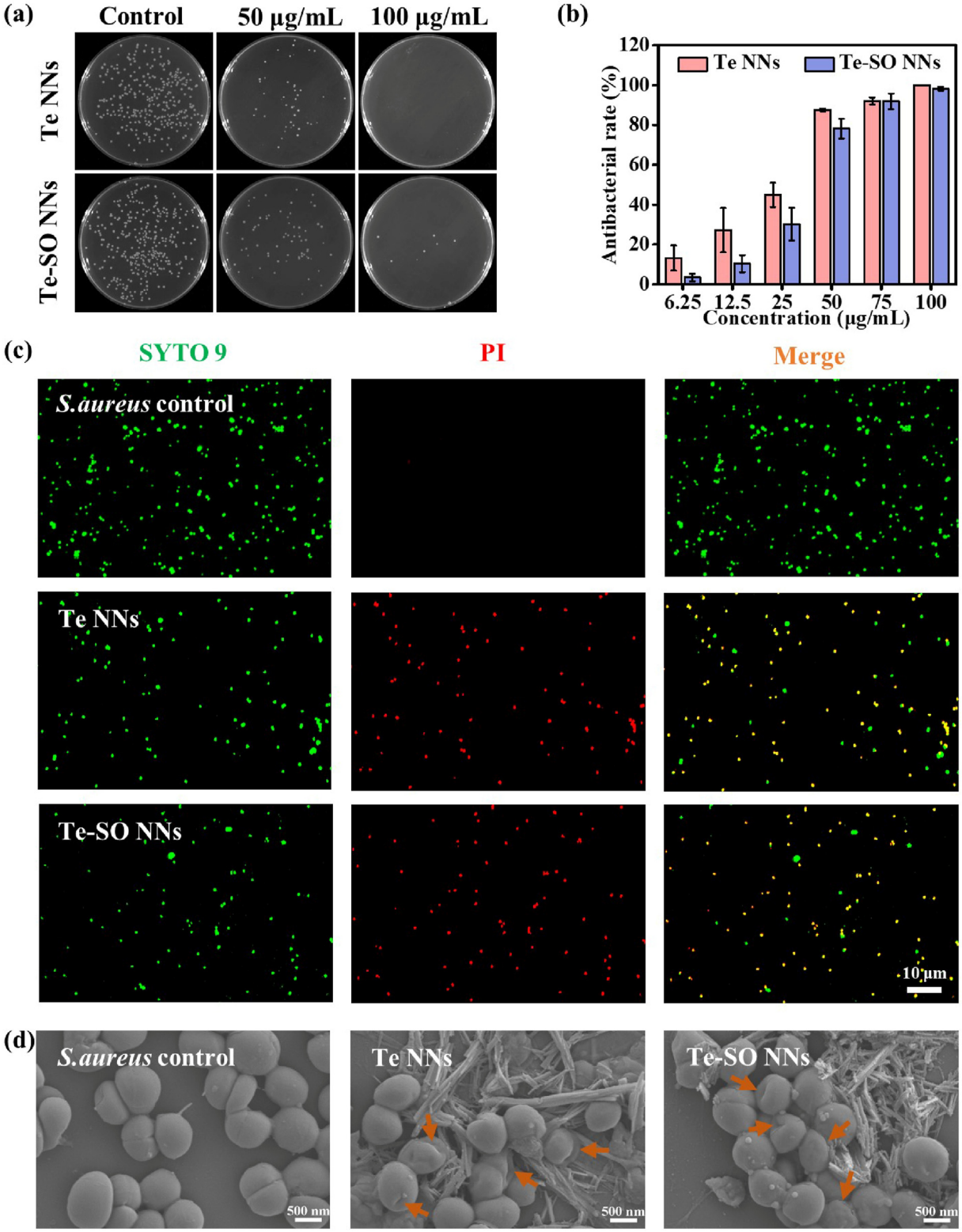

Fig. 3. Antibacterial activity of Te and Te–SO NNs toward *S. aureus*. (a) Variable numbers of colonies and (b) antibacterial rate in the presence of Te and Te–SO NNs at different concentrations. (c) SYTO 9/PI staining of *S. aureus* treated with Te and Te–SO NNs (100 μg mL^{-1}). (d) SEM images of *S. aureus* with the treatment of Te or Te–SO NNs (100 μg mL^{-1}).

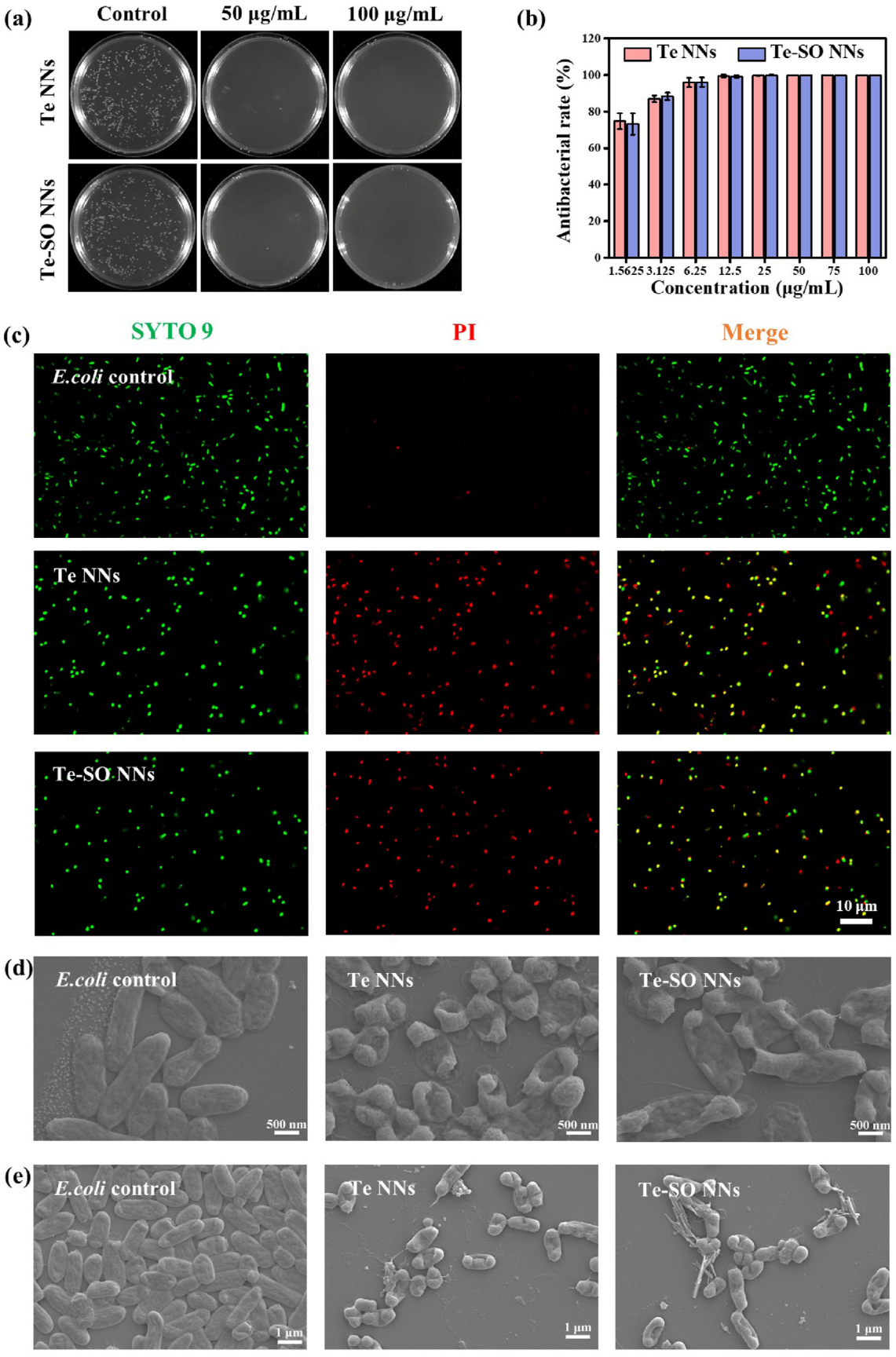

Fig. 4. Antibacterial and antibiofilm activity of Te and Te–SO NNs toward *E. coli*. (a) Variable numbers of colonies and (b) antibacterial rate in the presence of Te and Te–SO NNs at different concentrations. (c) SYTO 9/PI staining of *E. coli* treated with Te and Te–SO NNs (100 μg mL^{-1}). SEM images of (d) *E. coli* and (e) *E. coli* biofilms with the treatment of Te or Te–SO NNs (100 μg mL^{-1}).

with structurally intact cytoplasmic membranes, which only penetrates dead bacterial cells with disrupted membranes. These two dyes provide a rapid and reliable method for discriminating between live and dead bacteria. As performed in Fig. 3c, all bacteria are alive (stained by SYTO 9, green fluorescence) in the control group, while most of bacteria are dead (staining by PI, red fluorescence) after 24 h treatment of Te NNs and Te–SO NNs. This confirms the excellent *S. aureus* disinfection of Te NNs as well as Te–SO NNs. In addition, the morphology changes of *S. aureus* are visualized through SEM (Fig. 3d). The spherical well-dividing bacterial cells with intact membrane structure and smooth surface are observed in the control group. In comparison, the bacteria treated with Te and Te–SO NNs are shrunk and their membranes become incomplete, sunken, and even melted (orange arrow), which results in the leakage of cytoplasm and thereby causes the death of bacteria. Generally,

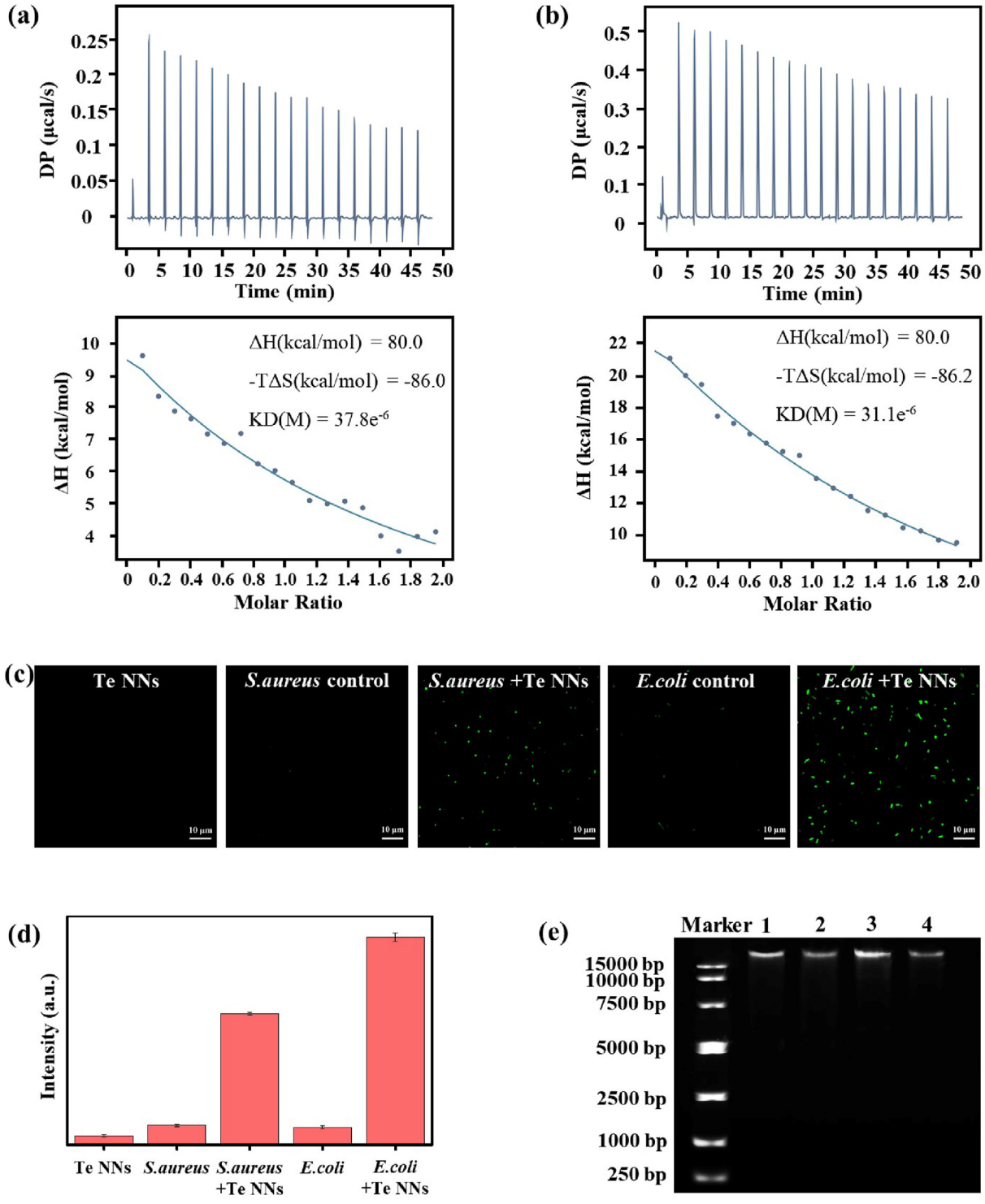

Fig. 5. Antibacterial mechanism of Te NNs. ITC spectra and fitting curve of Te NNs to (a) PG and (b) LPS. (c) Fluorescence images and (d) luminescence intensity of ROS in Te NNs group, *S. aureus* control group, *S. aureus*+Te NNs group, *E. coli* control group and *E. coli*+Te NNs group. (e) Bacterial agar gel electrophoresis profiles of genomic DNA obtained from direct DNA extracts of the samples; allelic bands were: Lane Marker, 15 000 bp DNA ladder; Lane 1, *S. aureus* control group; Lane 2, *S. aureus*+Te NNs group; Lane 3, *E. coli* control group; Lane 4, *E. coli*+Te NNs group.

antimicrobial resistance (AMR) will cause increased threat in clinic, hence the possible induced resistance of bacteria with long-term exposure to NNs is assessed. The results reveal that the prepared Te NNs exhibit retained antibacterial effects to the *S. aureus* during 25-day exposure (Figure S3).

3.4. Antibacterial and antibiofilm activity to E. coli

The antibacterial activity of NNs toward Gram-negative bacteria (*E. coli*) is illustrated in Fig. 4. The viable cell counting method is used to evaluate *E. coli* elimination ability of Te and Te–SO NNs (Fig. 4a). The results demonstrate that Te and Te–SO NNs can kill all *E. coli* even at the concentration of 50 μg mL^{-1} (Fig. 4a and b), illustrating a stronger antibacterial effect than against *S. aureus*. What's more, both Te and Te–SO NNs maintain excellent antibacterial efficiency *to E. coli* until the concentration drops to 1.5625 μg mL^{-1}. And as shown in Figure S4, the antibacterial efficiency of Te NNs also maintain at an ideal level with MIC of 3.125 μg mL^{-1} when dispersed in PBS for 6 months. Furthermore, Te NNs perform no detectable resistance after the serial incubation with the selected *E. coli* at sub-MIC over a 25-day period (Figure S5).

The SYTO 9/PI staining shown in Fig. 4c further confirms their bactericidal activity, in which the full-screen green is covered by red in 24 h of contact with 100 μg mL^{-1} NNs. The morphological change in *E. coli* cells caused by NNs is examined by SEM (Fig. 4d). The rod-shaped cells with intact cell membranes are investigated in the control group. However, when treated with Te and Te–SO NNs, a severe folding and shrinking of bacterial cytoplasm can be observed.

More importantly, *E. coli* can easily adhere to the surface of implants, then form mature and stable biofilms, which can prevent the penetration of both antibiotics and immune cells, leading to difficulty in bacteria eradication. *E. coli* biofilms are certainly the major cause of morbidity and mortality of bacterial infections [46,47]. To visualize the antibiofilm

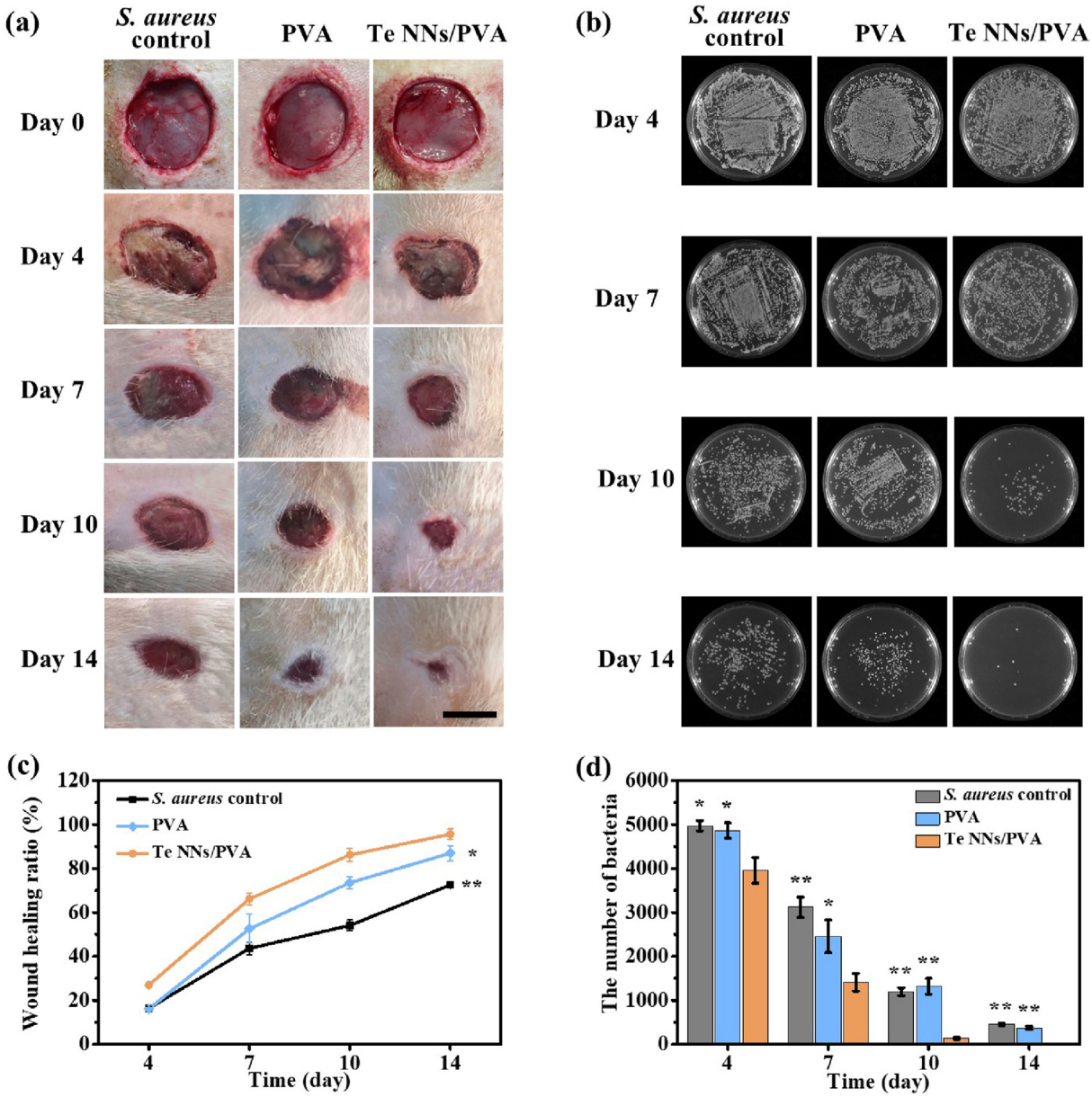

Fig. 6. Therapeutic effect of Te NNs/PVA hydrogel on *S. aureus* infected wounds *in vivo*. (a) Representative photographs of wounds treated with PBS, PVA hydrogel and Te NNs/PVA hydrogel at days 0, 4, 7, 10, and 14; scale bar, 1 cm. (b) Photographs of bacterial cultures taken from the skin tissue with different treatments during the same time period. (c) The wound healing ratio of rats from day 4 to day 14. (d) The number of residual bacteria at the wound sites of different treatment groups. Data are represented as mean ± standard deviation (n = 5 in each group); *p < 0.05, **p < 0.01 compared to the Te NNs/PVA group.

capability toward *E. coli* of the Te and Te–SO NNs, the *E. coli* biofilms treated with NNs are investigated. The SEM images in Fig. 4e show that bacterial biofilms in the control group are distributed evenly and grow densely. By contrast, the *E. coli* biofilms are significantly destructed with obvious changes of bacterial morphology in the presence of Te and Te–SO NNs, indicating excellent antibiofilm activity of the NNs to *E. coli* (Fig. 4e). Furthermore, the quantitative assessment for *E. coli* biofilm growth by MTT assay (Figure S8) shows that both Te and Te–SO NNs have significantly disrupted biofilm at the concentration of 100 μg mL^{-1} as compared to control group, which comfirms the outstanding antibiofilm activity of the NNs. The Te NNs and Te–SO NNs exhibit excellent antibiofilm activity in a relatively short period of 2 h with biofilm viability of 52.7% and 51.1%, respectively. When the treatment time is extended to 12 h, the biofilm viability is further reduced to respective 27.1% and 28.3%.

3.5. Antibacterial mechanism

The antibacterial activity discussed above shows the varying degrees of morphological damage caused by Te and Te–SO NNs. In general, the Gram-positive bacteria possess thick peptidoglycan (PG) layer and the lipopolysaccharide (LPS) accounts for a large portion in Gram-negative bacterial cell walls [48,49]. To further investigate the interaction process of Te NNs to PG and LPS, isothermal titration calorimetry (ITC) is applied and the resulting isotherm was fitted to a one-site binding model using the nonlinear Levenberg-Marquardt fitting algorithm by MicroCal PEAQ-ITC Analysis Software (Fig. 5a and b). The value of ΔH and ΔS is employed to determine the driving force during the interaction process which includes the van der Waals force, hydrophobic interactions and hydrogen bonds [50,51]. The ΔH and -TΔS of Te NNs to LPS and PG are almost the same, implying that the main driving force is similar in these two interaction processes. Moreover, the equilibrium dissociation constants (KD) of Te NNs to PG and LPS are respectively listed as $37.8e^{-6}$ and $31.1e^{-6}$, suggesting that Te NNs have a great affinity to PG as well as LPS. However, the ITC result of Te–SO NNs to PG performs insignificant endothermic or exothermic behavior (Figure S6a), which indicates that this binding ability attenuates with surface oxidation of Te NNs, therefore reducing the bactericidal ability to *S. aureus*. And the binding ability of Te and Te–SO NNs to PG is also confirmed using a PG kit. After the mixture of NNs with PG is shaken for 4 h at 4 °C, the binding rate of Te NNs to PG is nearly twice that of Te–SO NNs (Figure S6b).

In addition, the antibacterial activities of Te nanoparticles are

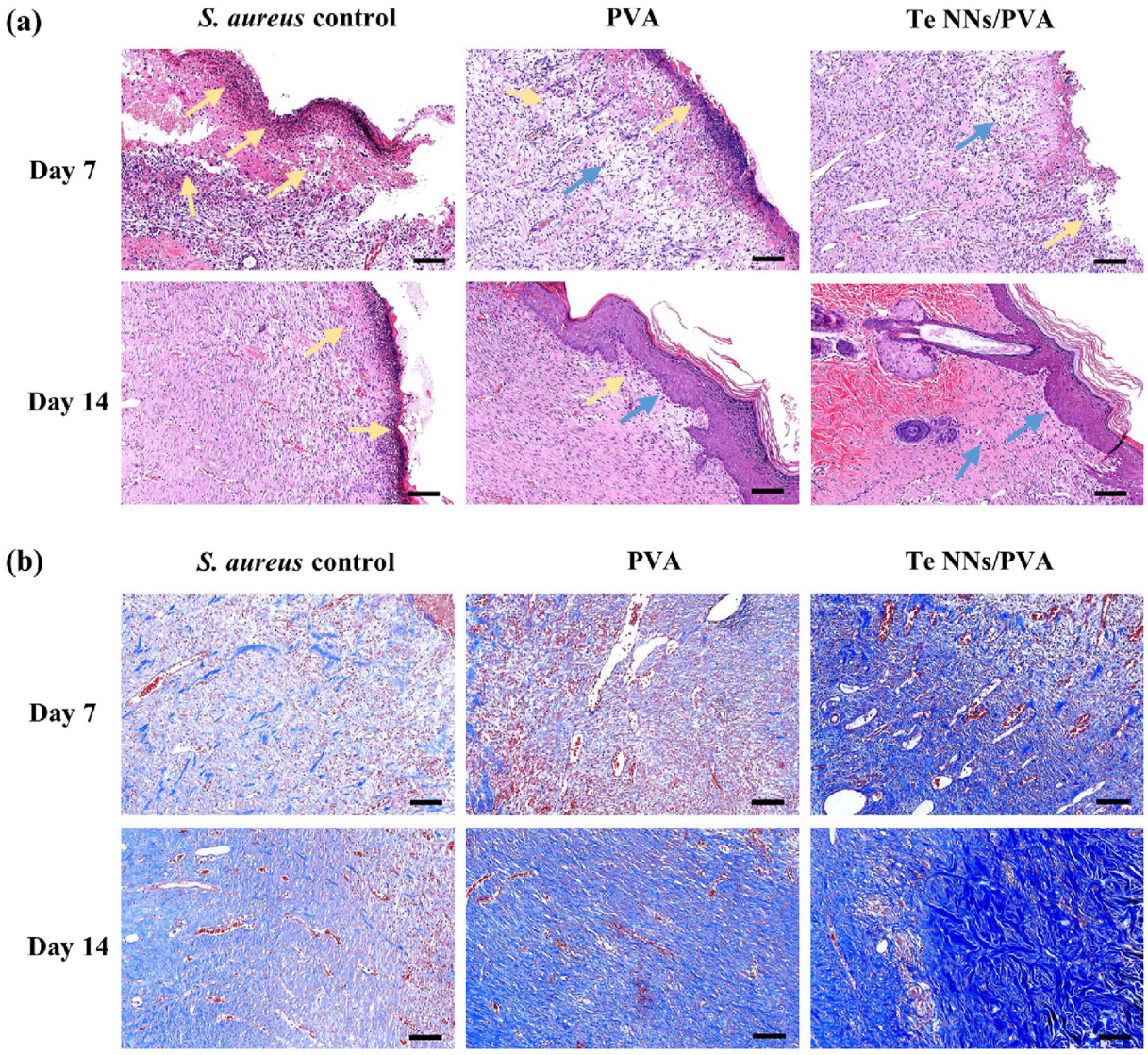

Fig. 7. The histological images of the skin tissue on *S. aureus* infected wounds. (a) H&E stained images and (b) Masson's staining images showing the degree of *S. aureus* infection of skin tissue after treating with different dressings for 7 and 14 days. Scale bar, 100 μm. Yellow arrows: neutrophils; Blue arrows: fibroblasts.

possibly related to the formation of ROS [35,52–54]. A high ROS level can increase oxidative stress in cells, which can damage both the cell membranes and the proteins, then cause bacterial death. Fluorescence images of ROS in Fig. 5c show green fluorescence in both *S. aureus* and *E. coli* with the treatment of Te NNs. Moreover, the *E.coli*+Te NNs group emits stronger green fluorescence, indicating more ROS generation, hence enhancing the sterilization ability. Nevertheless, the Te NNs per se emit negligible fluorescence of ROS, whose luminescence intensity is far lower than *S.aureus*+Te NNs and *E.coli*+Te NNs groups (Fig. 5c and d). Furthermore, after the introduction of Te NNs, the genomic levels of *S. aureus* and *E. coli* are all weaker than that of respective control group, especially for *E.coli*+Te NNs group. In general, the Te NNs cover and adhere to the surfaces of *S. aureus* and *E. coli* and further accelerate ROS generation of bacteria to cause membrane and DNA damage, finally eliminating the bacteria. Moreover, the better morphological damage and biofilms destruction ability toward *E. coli* may be owing to more ROS generation. And as shown in the green fluorescence in Figure S6c, the intracellular ROS of *S. aurues* stimulated by Te NNs is more than that stimulated by Te–SO NNs, contributing to better antibacterial ability to *S. aureus* of Te NNs. Compared to current antibacterial agents which promote ROS generation to eliminate bacteria under external stimuli (e.g. photo, sound, microwave) [55–59], the Te NNs perform more flexibility in the application.

We further investigate the SEM images (Figure S7) which shows the puncturing behavior of Te NNs. When the bacteria co-cultured with Te NNs, the nanoneedles have a contact with the bacterial cells and as shown in the partial enlarged views of Figure S7, the needle-like structure punctures bacterial membranes, visibly deforming the cells, especially the *E. coli* cells. Therefore, the antibacterial mechanism of Te NNs attributes to the chemical (ROS) damage as well as physical damage on bacteria.

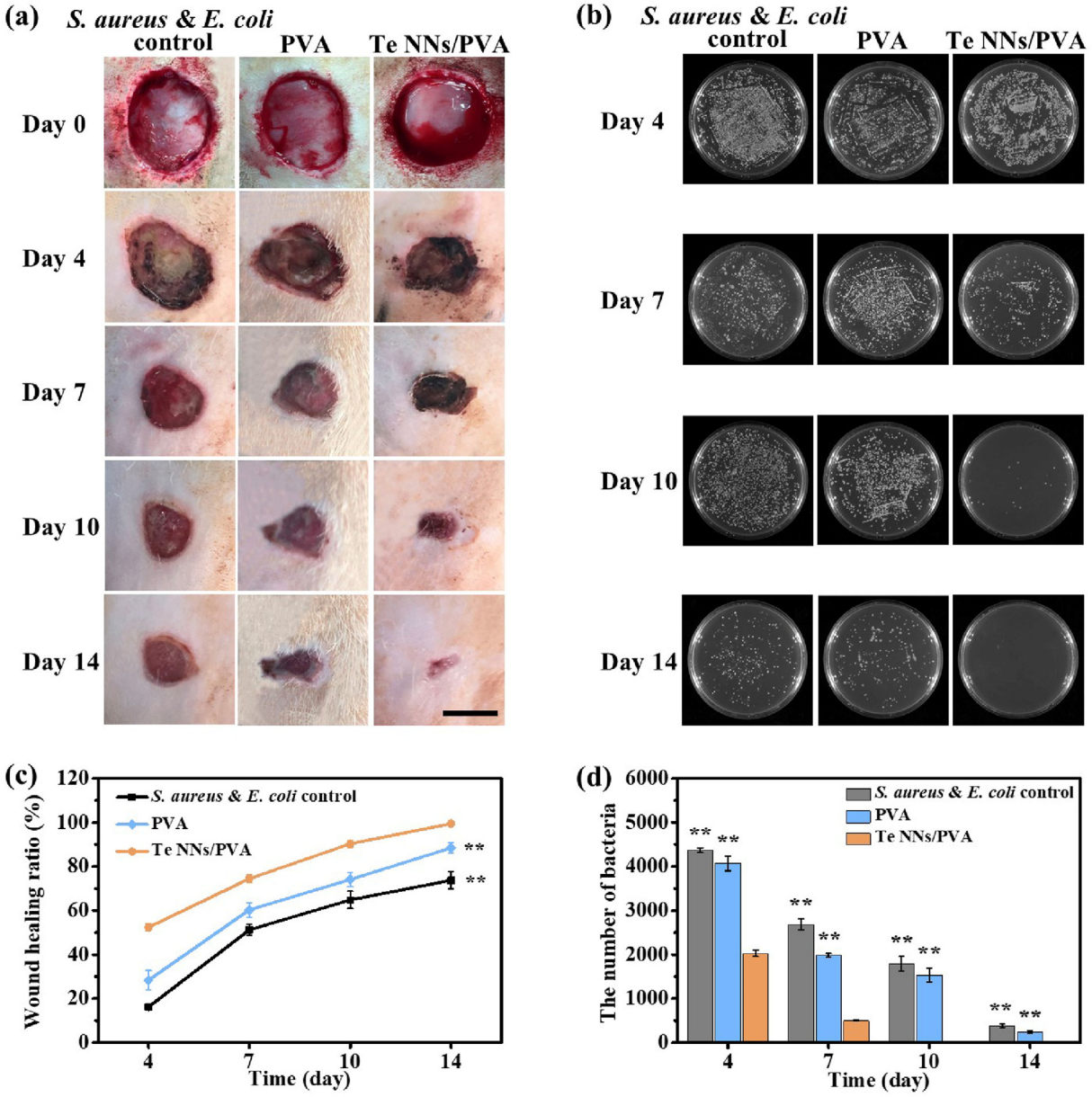

Fig. 8. Therapeutic effect of Te NNs/PVA hydrogel on *S. aureus & E. coli* co-infected wounds *in vivo*. (a) Representative photographs of wounds treated with PBS, PVA hydrogel and Te NNs/PVA hydrogel at days 0, 4, 7, 10, and 14; scale bar, 1 cm. (b) Photographs of bacterial cultures taken from the skin tissue with different treatments during the same time period. (c) The wound healing ratio of rats from day 4 to day 14. (d) The number of residual bacteria at the wound sites of different treatment groups. Data are represented as mean ± standard deviation (n = 5 in each group); *p < 0.05, **p < 0.01 compared to the Te NNs/PVA group.

3.6. Healing therapy for infected wounds

We establish *S. aureus* infected wound model by full-thickness skin wounds excision and immediate *S. aureus* infection. To confirm the *in vivo* antibacterial and wound healing applicability, the Te NNs/PVA hydrogel is prepared and placed on the wounds 24 h post-surgery. Fig. 6a records representative photographs of the wounds at different time points. The trauma in the control and PVA hydrogel groups presents a large area of unhealed skin defect with severe infection after 4 days of treatment, while the trauma in the Te NNs/PVA hydrogel group heals faster at each time point. To further confirm the sterilization ability of Te NNs/PVA hydrogel, the residual bacteria are collected from the wound and cultured in the NB agar plates. Densely packed colonies are observed in the control and PVA hydrogel groups even at the treatment of day 14 (Fig. 6b), which cause continuous exudate from the infected wounds, prolonging the healing process. Obviously, at each time point, the number of residual bacteria at the wounds treated with Te NNs/PVA hydrogel was apparently lower than the others (Fig. 6b,d). Especially after 14 days of treatment, the inflammation of wounds is eliminated, attributing to a better recovery from the bacterial infection with a healing ratio of 98% (Fig. 6a,c).

The H&E staining and Masson's trichrome staining of the infected wound tissue are performed to observe the re-epithelization, fibroblast immigration, connective tissue synthesis, infiltration of inflammatory cells and collagen production. After 7 days of treatment, the obvious neutrophil infiltration surrounding the wounds can be observed in the control and PVA hydrogel groups (Fig. 7a), which indicates a severe bacterial infection. In comparison, the Te NNs/PVA hydrogel group exhibits negligible neutrophils and more fibroblasts, thus confirming the wound healing effects of Te NNs. On the 14th day, except for the control group, the other two groups form a layer of complete epithelium. Moreover, the Te NNs/PVA hydrogel group exhibits the maximum amount of mature blood vessels, hair follicles and well-proliferated fibroblasts, demonstrating the best wound healing effect. The formation and distribution of collagen on wounds are evaluated using Masson's trichrome staining in Fig. 7b. The shade of blue in the Te NNs/PVA hydrogel group is apparently darker than the other two groups after both 7 days and 14 days of treatment, revealing Te NNs/PVA can improve

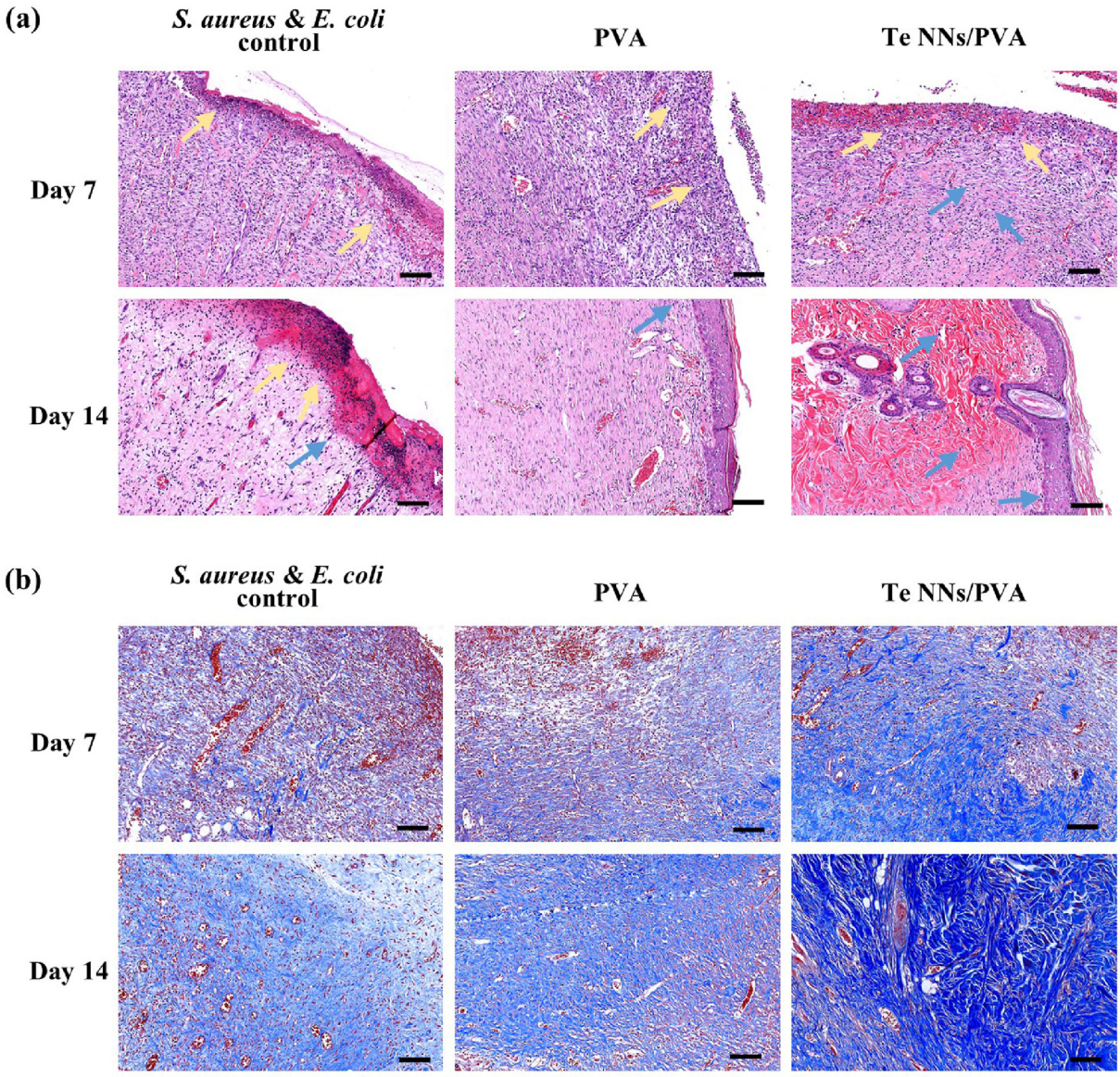

Fig. 9. The histological images of the skin tissue on *S. aureus & E. coli* co-infected wounds. (a) H&E stained images and (b) Masson's staining images. The results show the degree of *S. aureus & E. coli* co-infection of skin tissue after treating with different dressings for 7 and 14 days. Scale bar, 100 μm. Yellow arrows: neutrophils; Blue arrows: fibroblasts.

collagen formation to accelerate the wound healing process.

Furthermore, *S. aureus* and *E. coli* co-infected wound model is also established to assess the antibacterial ability of Te NNs *in vivo* since mixed bacterial infection is more likely to cause severe consequences, hindering wound healing [60,61]. Fig. 8a shows a large area of skin defect with inflammation, suppuration, and ulceration in the control group during the first week post-surgery. As for Te NNs/PVA hydrogel group, the trauma becomes dry and scab at day 4 and is healed completely after 14 days of treatment, whereas the control and PVA hydrogel groups do not heal well with a remaining area (Fig. 8a,c). The bacteria residues in wounds further confirm the bacterial elimination ability of Te NNs as the negligible colonies can be observed in the Te NNs/PVA hydrogel group on the tenth day (Fig. 8b,d). However, bacterial infection still exists in the control and PVA groups even after 14 days of treatment.

The wound skin tissues of the three group mice are obtained and stained by H&E on days 7 and 14 (Fig. 9a). In the control and PVA groups, a lot of white blood cells are produced at the 7 days of infection and they mainly existed as neutrophils, demonstrating the inflammatory response by *S. aureus* and *E. coli*. And the congestion appears notably in the control group due to serious inflammation. In the following days, the fibroblasts increase with the decreasing of neutrophils and the squamous epithelium forms during the healing process. In the Te NNs/PVA hydrogel group, the foci almost disappear and the neonatal tissues are smooth at day 14. Simultaneously, a large number of intact capillaries filled with red blood cells appear, proving the excellent treatment effect of Te NNs/PVA hydrogel. The blue staining in Fig. 9b shows that Te NNs/PVA hydrogel group performs a higher density of collagen compared to the control and PVA hydrogel groups at days 7 and 14. Moreover, after 14 days of treatment, the newly formed collagen fibers of the wounds in Te NNs/PVA hydrogel group have a perfect fusion with normal tissues, indicating that Te NNs/PVA hydrogel is conductive to collagen formation, thus promoting wound healing.

In addition, the H&E staining images of the main organs including heart, liver, spleen, lung, and kidney in the control and treated groups are depicted in Fig. 10. In both the *S. aureus* infected and *S. aureus* & *E. coli* co-infected model, Te NNs/PVA hydrogel has no hazards to major organs since the H&E sections of the heart, liver, spleen, lung, and kidney in the treatment group show no obvious histological changes compared to control group. Therefore, Te NNs/PVA hydrogel provides a safe and effective strategy for the treatment of infected wounds.

4. Conclusions

In conclusion, a kind of biocompatible Te NNs is synthesized by a facile method for long-term stable antibacterial application. The as-prepared Te NNs are inherently inert to ROS generation and also do not stimulate the generation of ROS in mammalian cells, which exhibits low cytotoxicity. It is found that the biocompatible Te NNs can adhere to the surface of *S. aureus* and *E. coli* and subsequently promote the generation of ROS in bacteria and the needle-like structure can cause the physical damage of bacterial membranes, which results in excellent antibacterial ability. Moreover, this bacteria-killing activity is still maintained at a high level with the surface oxidation of Te NNs in PBS

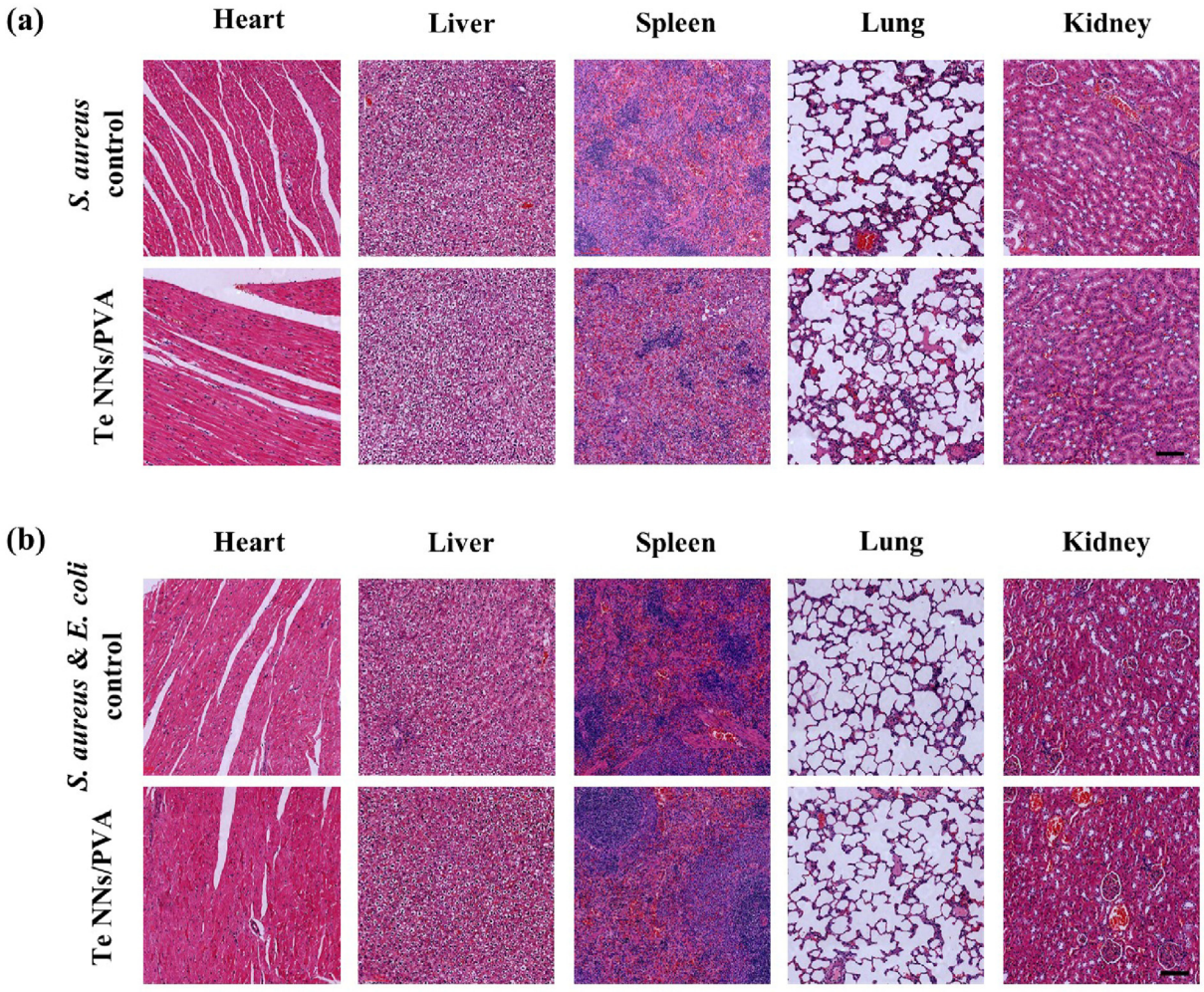

Fig. 10. H&E staining of the heart, liver, spleen, lung, kidney tissue slices of different treatment groups after 14 days. Scale bar, 100 μm.

even for 6 months. Furthermore, *in vivo* wound therapeutic results demonstrate that the Te NNs/PVA hydrogel can eliminate bacteria as well as promote wound healing. We believe this work helps us understand the antibacterial behaviors of Te NNs and deliver effective therapeutic guidance for application in infectious diseases.

Credit author statement

Lihua Li: Supervision and guidance. **Zhijun Ma**: Supervision and guidance. **Ling Huang**: Materials preparation, characterization analysis, biological examination, animal related experiments, data curation, writing – original draft. **Meng Liu**: Materials preparation, characterization analysis, biological examination, writing-supplement. **Zhibin Feng**: Animal related experiments. **Xingyi Xu**: Characterization analysis. **Lingling Chen**: Animal related experiments.

Declaration of competing interest

The authors declare that they have no conflict of interest.

Acknowledgments

This work was financially supported by the National Natural Science Foundation of China (52002133, 61927816, U1609219, 51872095), Key R&D Program of Guangzhou (No. 202007020003), Research Project of Zhejiang Lab (No. 113014-AC2101), the Fundamental Research Funds for the Central Universities (2019MS126) and State Key Lab of Luminescent Materials and Devices.

Appendix A. Supplementary data

Supplementary data to this article can be found online at https://doi.org/10.1016/j.mtbio.2022.100271.

References

[1] F. Baino, S. Ferraris, M. Miola, S. Perero, E. Verne, A. Coggiola, D. Dolcino, M. Ferraris, Novel antibacterial ocular prostheses: proof of concept and physico-chemical characterization, Mater. Sci. Eng. C Mater. Biol. Appl. 60 (2016) 467–474, https://doi.org/10.1016/j.msec. 2015.11.075.

[2] S. Calamak, C. Erdogdu, M. Ozalp, K. Ulubayram, Silk fibroin based antibacterial bionanotextiles as wound dressing materials, Mater. Sci. Eng. C Mater. Biol. Appl. 43 (2014) 11–20, https://doi.org/10.1016/j.msec.2014.07.001.

[3] M.J. Hajipour, K.M. Fromm, A. Akbar Ashkarran, D. Jimenez de Aberasturi, I.R.d. Larramendi, T. Rojo, V. Serpooshan, W.J. Parak, M. Mahmoudi, Antibacterial properties of nanoparticles, Trends Biotechnol. 30 (2012) 499–511, https://doi.org/10.1016/j.tibtech. 2012.06.004.

[4] L. Liu, H. Shi, H. Yu, S. Yan, S. Luan, The recent advances in surface antibacterial strategies for biomedical catheters, Biomater. Sci. 8 (2020) 4095–4108, https://doi.org/10.1039/D0BM00659A.

[5] X. Wang, H. Fan, F. Zhang, S. Zhao, Y. Liu, Y. Xu, R. Wu, D. Li, Y. Yang, L. Liao, H. Zhu, X. Wang, Antibacterial properties of bilayer biomimetic nano-ZnO for dental implants, ACS Biomater. Sci. Eng. 6 (2020) 1880–1886, https://doi.org/10.1021/acsbiomaterials.9b01695.

[6] E.M. Ory, E.M. Yow, The use and abuse of the broad spectrum antibiotics, JAMA 185 (1963) 273–279, https://doi.org/10.1001/jama.1963.03060040057022.

[7] A. Finn, N. Curtis, A.J. Pollard, Hot Topics in Infection and Immunity in Children VI, Springer, 2010, https://doi.org/10.1007/978-1-4419-0981-7.

[8] L. Rizzello, R. Cingolani, P.P. Pompa, Nanotechnology tools for antibacterial materials, Nanomedicine 8 (2013) 807–821, https://doi.org/10.2217/nnm.13.63.

[9] S. Tang, J. Zheng, Antibacterial activity of silver nanoparticles: structural effects, Adv. Healthc. Mater. 7 (2018) 1701503, https://doi.org/10.1002/adhm.201701503.

[10] K. Giannousi, A. Pantazaki, C. Dendrinou-Samara, Copper-based Nanoparticles as antimicrobials//Nanostructures for Antimicrobial Therapy, Elsevier, 2017, pp. 515–529, https://doi.org/10.1016/B978-0-323-46152-8.00023-8.

[11] S. Yao, X. Feng, J. Lu, Y. Zheng, X. Wang, A.A. Volinsky, L.N. Wang, Antibacterial activity and inflammation inhibition of ZnO nanoparticles embedded TiO_2 nanotubes, Nanotechnology 29 (2018) 244003, https://doi.org/10.1088/1361-6528/aabac1.

[12] L.E. Shi, Z.H. Li, W. Zheng, Y.F. Zhao, Y.F. Jin, Z.X. Tang, Synthesis, antibacterial activity, antibacterial mechanism and food applications of ZnO nanoparticles: a review, Food Addit. Contam. Part A Chem. Anal. Control Expo. Risk Assess. 31 (2014) 173–186, https://doi.org/10.1080/19440049.2013.865147.

[13] M.N. Alomary, M.A. Ansari, Proanthocyanin-capped biogenic TiO_2 nanoparticles with enhanced penetration, antibacterial and ROS mediated inhibition of bacteria proliferation and biofilm formation: a comparative approach, Chemistry 27 (2021) 5817–5829, https://doi.org/10.1002/chem.202004828.

[14] C. Mao, Y. Xiang, X. Liu, Z. Cui, X. Yang, K.W.K. Yeung, H. Pan, X. Wang, P. Chu, S. Wu, Photo-inspired antibacterial activity and wound healing acceleration by hydrogel embedded with Ag/Ag@ AgCl/ZnO nanostructures, ACS Nano 11 (2017) 9010–9021, https://doi.org/10.1021/acsnano.7b03513.

[15] C. Mao, Y. Xiang, X. Liu, Z. Cui, X. Yang, Z. Li, S. Zhu, Y. Zheng, K.W.K. Yeung, S. Wu, Repeatable photodynamic therapy with triggered signaling pathways of fibroblast cell proliferation and differentiation to promote bacteria-accompanied wound healing, ACS Nano 12 (2018) 1747–1759, https://doi.org/10.1021/acsnano.7b08500.

[16] Y. Li, X. Liu, B. Li, Y. Zheng, Y. Han, D. Chen, K.W.K. Yeung, Z. Cui, Y. Liang, Z. Li, S. Zhu, X. Wang, S. Wu, Near-infrared light triggered phototherapy and immunotherapy for elimination of methicillin-resistant Staphylococcus aureus biofilm infection on bone implant, ACS Nano 14 (2020) 8157–8170, https://doi.org/10.1021/acsnano.0c01486.

[17] B. Huang, L. Tan, X. Liu, J. Li, S. Wu, A facile fabrication of novel stuff with antibacterial property and osteogenic promotion utilizing red phosphorus and near-infrared light, Bioact. Mater. 4 (2019) 17–21, https://doi.org/10.1016/j.bioactmat.2018.11.002.

[18] M. Schieber, N.S. Chandel, ROS function in redox signaling and oxidative stress, Curr. Biol. 24 (2014) R453–R462, https://doi.org/10.1016/j.cub.2014.03.034.

[19] J. Zhang, Y. Fu, P. Yang, X. Liu, Y. Li, Z. Gu, ROS scavenging biopolymers for anti-inflammatory diseases: classification and formulation, Adv. Mater. Interfac. 7 (2020) 2000632, https://doi.org/10.1002/admi.202000632.

[20] J. Li, Z. Li, X. Liu, C. Li, Y. Zheng, K.W.K. Yeung, Z. Cui, Y. Liang, S. Zhu, W. Hu, Y. Qi, T. Zhang, X. Wang, S. Wu, Interfacial engineering of $Bi_2S_3/Ti_3C_2T_x$ MXene based on work function for rapid photo-excited bacteria-killing, Nat. Commun. 12 (2021) 1224, https://doi.org/10.1038/s41467-021-21435-6.

[21] Y. Xiang, Q. Zhou, Z. Li, Z. Cui, X. Liu, Y. Liang, S. Zhu, Y. Zheng, K.W.K. Yeung, S. Wu, A Z-scheme heterojunction of ZnO/CDots/C_3N_4 for strengthened photoresponsive bacteria-killing and acceleration of wound healing, J. Mater. Sci. Technol. 57 (2020) 1–11, https://doi.org/10.1016/j.jmst.2020.05.016.

[22] Y. Li, X. Liu, L. Tan, Z. Cui, X. Yang, Y. Zheng, K.W.K. Yeung, P.K. Chu, S. Wu, Rapid sterilization and accelerated wound healing using Zn^{2+} and graphene oxide modified g-C_3N_4 under dual light irradiation, Adv. Funct. Mater. 28 (2018) 1800299, https://doi.org/10.1002/adfm.201800299.

[23] H. Ding, D. Han, Y. Han, Y. Liang, X. Liu, Z. Li, S. Zhu, S. Wu, Visible light responsive CuS/protonated g-C_3N_4 heterostructure for rapid sterilization, J. Hazard Mater. 393 (2020) 122423, https://doi.org/10.1016/j.jhazmat.2020.122423.

[24] D. Han, Y. Li, X. Liu, K.W.K. Yeung, Y. Zheng, Z. Cui, Y. Liang, Z. Li, S. Zhu, X. Wang, S. Wu, Photothermy-strengthened photocatalytic activity of polydopamine-modified metal-organic frameworks for rapid therapy of bacteria-infected wounds, J. Mater. Sci. Technol. 62 (2021) 83–95, https://doi.org/10.1016/j.jmst.2020.05.055.

[25] A. Taylor, Biochemistry of tellurium, Biol. Trace Elem. Res. 55 (1996) 231–239, https://doi.org/10.1007/BF02785282.

[26] Z.H. Lin, C.H. Lee, H.Y. Chang, H.T. Chang, Antibacterial activities of tellurium nanomaterials, Chem. Asian J. 7 (2012) 930–934, https://doi.org/10.1002/asia.201101006.

[27] B. Zare, M.A. Faramarzi, Z. Sepehrizadeh, M. Shakibaie, S. Rezaie, A.R. Shahverdi, Biosynthesis and recovery of rod-shaped tellurium nanoparticles and their bactericidal activities, Mater. Res. Bull. 47 (2012) 3719–3725, https://doi.org/10.1016/j.materresbull. 2012.06.034.

[28] W. Wang, B. Li, H. Yang, Z. Lin, L. Chen, Z. Li, J. Ge, T. Zhang, H. Xia, L. Li, Y. Lu, Efficient elimination of multidrug-resistant bacteria using copper sulfide nanozymes anchored to graphene oxide nanosheets, Nano Res. 13 (2020) 2156–2164, https://doi.org/10.1007/s12274-020-2824-7.

[29] W. Wang, X. Cheng, J. Liao, Z. Lin, L. Chen, D. Liu, T. Zhang, L. Li, Y. Lu, H. Xia, Synergistic photothermal and photodynamic therapy for effective implant-related bacterial infection elimination and biofilm disruption using Cu_9S_8 nanoparticles, ACS Biomater. Sci. Eng. 5 (2019) 6243–6253, https://doi.org/10.1021/acsbiomaterials.9b01280.

[30] W.J. Lan, S.H. Yu, H.S. Qian, Y. Wan, Dispersibility, stabilization, and chemical stability of ultrathin tellurium nanowires in acetone: morphology change, crystallization, and transformation into TeO_2 in different solvents, Langmuir 23 (2007) 3409–3417, https://doi.org/10.1021/la063272+.

[31] F. Li, T. Li, W. Cao, L. Wang, H. Xu, Near-infrared light stimuli-responsive synergistic therapy nanoplatforms based on the coordination of tellurium-containing block polymer and cisplatin for cancer treatment, Biomaterials 133 (2017) 208–218, https://doi.org/10.1016/j.biomaterials.2017.04.032.

[32] Q. Lu, F. Gao, S. Komarneni, Biomolecule-Assisted reduction in the synthesis of single-crystalline tellurium nanowires, Adv. Mater. 16 (2004) 1629–1632, https://doi.org/10.1002/adma.200400319.

[33] Q. Lu, F. Gao, S. Komarneni, A green chemical approach to the synthesis of tellurium nanowires, Langmuir 21 (2005) 6002–6005, https://doi.org/10.1021/la050594p.

[34] A.V. Crua, D. Medina, B. Zhang, M.U. González, Y. Huttel, J.M. García-Martín, J.L. Cholula-Díaz, T.J. Webster, Comparison of cytocompatibility and anticancer properties of traditional and green chemistry-synthesized tellurium nanowires, Int. J. Nanomed. 14 (2019) 3155–3176, https://doi.org/10.2147/IJN.S175640.

[35] D.M. Cruz, W. Tien-Street, B. Zhang, X. Huang, A.V. Crua, A. Nieto-Argüello, J.L. Cholula-Díaz, L. Martínez, Y. Huttel, M.U. González, J.M. García-Martín, T.J. Webster, Citric juice-mediated synthesis of tellurium nanoparticles with

antimicrobial and anticancer properties, Green Chem. 21 (2019) 1982–1998, https://doi.org/10.1039/C9GC00131J.
[36] Z. He, Y. Yang, J.W. Liu, S.H. Yu, Emerging tellurium nanostructures: controllable synthesis and their applications, Chem. Soc. Rev. 46 (10) (2017) 2732–2753, https://doi.org/10.1039/C7CS00013H.
[37] H.H. Li, P. Zhang, C.L. Liang, J. Yang, M. Zhou, X.H. Lu, G.A. Hope, Facile electrochemical synthesis of tellurium nanorods and their photoconductive properties, Cryst. Res. Technol. 47 (2012) 1069–1074, https://doi.org/10.1002/crat.201200273.
[38] J.W. Liu, F. Chen, M. Zhang, H. Qi, C.L. Zhang, S.H. Yu, Rapid microwave-assisted synthesis of uniform ultralong Te nanowires, optical property, and chemical stability, Langmuir 26 (2010) 11372–11377, https://doi.org/10.1021/la100772n.
[39] J.-K. Qin, P.-Y. Liao, M. Si, S. Gao, G. Qiu, J. Jian, Q. Wang, S.-Q. Zhang, S. Huang, A. Charnas, Y. Wang, M.J. Kim, W. Wu, X. Xu, H.-Y. Wang, L. Yang, Y. Khin Yap, P.D. Ye, Raman response and transport properties of tellurium atomic chains encapsulated in nanotubes, Nat. Electron. 3 (2020) 141–147, https://doi.org/10.1038/s41928-020-0365-4.
[40] A.P. Mirgorodsky, T. Merle-Méjean, J.C. Champarnaud, P. Thomas, B. Frit, Dynamics and structure of TeO_2 polymorphs: model treatment of paratellurite and tellurite; Raman scattering evidence for new γ-and δ-phases, J. phys. chem. solids 61 (2000) 501–509, https://doi.org/10.1016/S0022-3697(99)00263-2.
[41] J.W. Liu, J.H. Zhu, C.L. Zhang, H.W. Liang, S.H. Yu, Mesostructured assemblies of ultrathin superlong tellurium nanowires and their photoconductivity, J. Am. Chem. Soc. 132 (2010) 8945–8952, https://doi.org/10.1021/ja910871s.
[42] S.U. Egarievwe, E.D. Lukosi, I.O. Okwechime, R. Gul, A. Hossain, R.B. James, Effects of tellurium oxide on surface current and performance of CdZnTe nuclear radiation detectors, in: 2017 IEEE Nuclear Science Symposium and Medical Imaging Conference (NSS/MIC), IEEE, 2017, pp. 1–4, https://doi.org/10.1109/NSSMIC.2017.8532704.
[43] Y. Cheng, F. Yang, G. Xiang, K. Zhang, Y. Cao, D. Wang, H. Dong, X. Zhang, Ultrathin tellurium oxide/ammonium tungsten bronze nanoribbon for multimodality imaging and second near-infrared region photothermal therapy, Nano Lett. 19 (2019) 1179–1189, https://doi.org/10.1021/acs.nanolett.8b04618.
[44] H. Kong, J.-B. Yeo, H.-Y. Lee, A Study on the properties of tellurium-oxide thin films based on the variable sputtering gas ratio, J. Kor. Phys. Soc. 66 (2015) 1744–1749, https://doi.org/10.3938/jkps.66.1744.
[45] T. Groth, P. Falck, R.R. Miethke, Cytotoxicity of biomaterials—basic mechanisms and in vitro test methods: a review, Altern. Lab. Anim. 23 (1995) 790–799, https://doi.org/10.1177/026119299502300609.
[46] T. Romeo, Bacterial Biofilms, Springer, 2008, p. 322, https://doi.org/10.1007/978-3-540-75418-3.
[47] G. Sharma, S. Sharma, P. Sharma, D. Chandola, S. Dang, S. Gupta, R. Gabrani, Escherichia coli biofilm: development and therapeutic strategies, J. Appl. Microbiol. 121 (2016) 309–319, https://doi.org/10.1111/jam.13078.
[48] H.R. Kaback, [13] bacterial membranes, Method. enzymol. 22 (1971) 99–120, https://doi.org/10.1016/0076-6879(71)22015-2.
[49] A. Mai-Prochnow, M. Clauson, J. Hong, A.B. Murphy, Gram positive and Gram negative bacteria differ in their sensitivity to cold plasma, Sci. Rep. 6 (2016) 38610, https://doi.org/10.1038/srep38610(2016).
[50] A. Velázquez-Campoy, H. Ohtaka, A. Nezami, S. Muzammil, E. Freire, Isothermal titration calorimetry, Curr. Protoc. Cell Biol. 23 (2004) 17.8.1–17.8.24, https://doi.org/10.1002/0471143030.cb1708s23.
[51] D. Prozeller, S. Morsbach, K. Landfester, Isothermal titration calorimetry as a complementary method for investigating nanoparticle–protein interactions, Nanoscale 11 (2019) 19265–19273, https://doi.org/10.1039/C9NR05790K.
[52] L.A. Ba, M. Döring, V. Jamier, C. Jacob, Tellurium: an element with great biological potency and potential, Org. Biomol. Chem. 8 (2010) 4203–4216, https://doi.org/10.1039/c0Ob00086h.
[53] T.M. Chou, Y.Y. Ke, Y.H. Tsao, Y.C. Li, Z.H. Lin, Fabrication of Te and Te-Au nanowires-based carbon fiber fabrics for antibacterial applications, Int. J. Environ. Res. Publ. Health 13 (2016) 202, https://doi.org/10.3390/ijerph13020202.
[54] D. Medina-Cruz, A. Vernet-Crua, E. Mostafavi, M.U. González, L. Martínez, A.D. Jones, M. Kusper, E. Sotelo, M. Gao, L.D. Geoffrion, V. Shah, G. Guisbiers, J.L. Cholula-Díaz, C. Guillermier, F. Khanom, Y. Huttel, J.M. García-Martín, T.J. Webster, Aloe vera-mediated Te nanostructures: highly potent antibacterial agents and moderated anticancer effects, Nanomaterials 11 (2021) 514, https://doi.org/10.3390/nano11020514.
[55] Q. Zheng, X. Liu, Y. Zheng, K.W.K. Yeung, Z. Cui, Y. Liang, Z. Li, S. Zhu, X. Wang, S. Wu, The recent progress on metal–organic frameworks for phototherapy, Chem. Soc. Rev. 50 (2021) 5086–5125, https://doi.org/10.1039/D1CS00056J.
[56] Y. Ren, H. Liu, X. Liu, Y. Zheng, Z. Li, C. Li, K.W.K. Yeung, S. Zhu, Y. Liang, Z. Cui, S. Wu, Photoresponsive materials for antibacterial applications, Cell Rep. Phys. Sci. 1 (2020) 100245, https://doi.org/10.1016/j.xcrp.2020.100245.
[57] W. Guan, L. Tan, X. Liu, Z. Cui, Y. Zheng, K.W.K. Yeung, D. Zheng, Y. Liang, Z. Li, S. Zhu, X. Wang, S. Wu, Ultrasonic interfacial engineering of red phosphorous-metal for eradicating MRSA infection effectively, Adv. Mater. 33 (2021) 2006047, https://doi.org/10.1002/adma.202006047.
[58] J. Fu, Y. Li, Y. Zhang, Y. Liang, Y. Zheng, Z. Li, S. Zhu, C. Li, Z. Cui, S. Wu, An engineered pseudo-macrophage for rapid treatment of bacteria-infected osteomyelitis via microwave-excited anti-infection and immunoregulation, Adv. Mater. 33 (2021) 2102926, https://doi.org/10.1002/adma.202102926.
[59] Y. Qiao, X. Liu, B. Li, Y. Han, Y. Zheng, K.W.K. Yeung, C. Li, Z. Cui, Y. Liang, Z. Li, S. Zhu, X. Wang, S. Wu, Treatment of MRSA-infected osteomyelitis using bacterial capturing, magnetically targeted composites with microwave-assisted bacterial killing, Nat. Commun. 11 (2020) 1–13, https://doi.org/10.1038/s41467-020-18268-0.
[60] C. Zhao, X. Wang, L. Yu, L. Wu, X. Hao, Q. Liu, L. Lin, Z. Huang, Z. Ruan, S. Weng, A. Liu, X. Lin, Quaternized carbon quantum dots with broad-spectrum antibacterial activity for the treatment of wounds infected with mixed bacteria, Acta Biomater. 138 (2022) 528–544, https://doi.org/10.1016/j.actbio.2021.11.010.
[61] X. Hao, L. Huang, C. Zhao, S. Chen, W. Lin, Y. Lin, L. Zhang, A. Sun, C. Miao, X. Lin, M. Chen, S. Weng, Antibacterial activity of positively charged carbon quantum dots without detectable resistance for wound healing with mixed bacteria infection, Mater. Sci. Eng. C 123 (2021) 111971, https://doi.org/10.1016/j.msec.2021.111971.